Catalysis Science & Technology

Propane oxidative dehydrogenation using CO2 over CrOx/Fe-CeO2 catalysts

Journal:	*Catalysis Science & Technology*
Manuscript ID	CY-ART-09-2022-001563.R1
Article Type:	Paper
Date Submitted by the Author:	26-Jan-2023
Complete List of Authors:	Wang, Hedun; Rutgers University Department of Chemical and Biochemical Engineering Nguyen, Thu; Rutgers University Department of Chemical and Biochemical Engineering Tsilomelekis, George; Rutgers University Department of Chemical and Biochemical Engineering

ARTICLE

Propane oxidative dehydrogenation using CO_2 over CrO_x/Fe-CeO_2 catalysts

Received 00th January 20xx,
Accepted 00th January 20xx

DOI: 10.1039/x0xx00000x

Hedun Wang [a], Thu D. Nguyen [a] and George Tsilomelekis* [a]

The kinetic behavior of CrO_x sites supported on Fe doped CeO_2 was studied for the CO_2-assissted propane oxidative dehydrogenation. The support was synthesized via a co-precipitation method of Fe and Ce precursors while wetness impregnation was used to deposit the CrO_x species. XRD and Raman analysis confirmed the presence of dispersed CrO_x sites on the surface of the support at low loading while small Cr_2O_3 nanoparticles were found at high loadings. The addition of CrO_x sites reconstructs the available surface oxygen sites and enhances the reducibility of the catalyst as confirmed by H_2-TPR measurements. Herein we show that the CrO_x based catalysts outperform the parent support at low reaction temperatures both from a propane conversion and propylene selectivity perspective. At elevetated temperatures the effect of CrO_x sites on the propylene production diminishes since propane dry reforming dominates. A Langmuir-Hinshelwood kinetic model was developed based on 14 elementary steps to account for the dominating reaction pathways, i.e. propane dehydrogenation, reverse water gas shift and dry reforming. The regressed kinetic data showed that the incorpration of CrO_x on the support decreases the activation energy of the propane dehydrogenation by 60-75% while small decrease in the activation energy of dry reforming was noted (~15%).

Introduction

Over the past decade, the US shale gas revolution has played a profound role on the structure of domestic energy and chemical sectors. Recent reports have shown an increase in propane production with the advent of shale gas revolution which in turn directly provides propane at a reduced price as compared to expensive crude oil derivatives[1-3]. The shift to cheap chemical feedstocks offers an incentive for the research community to develop new technologies for propane conversion into value added products. Particularly, 'on-purpose' propylene production has already been successfully applied into industrial manufacture featured by Honeywell UOP process[4, 5]. Although propane conversion via direct dehydrogenation (PDH) is the widely used approach, it suffers from important challenges. The highly endothermic character generally requires vast energy input. In addition, propane conversion is limited due to thermodynamic equilibrium of PDH reaction, thus a separation and recycling of reactants from reactor downstream to upstream seems crucial to achieve high productivity. Apart from these potential drawbacks, product separation and catalyst regeneration techniques are essential in order to overcome product selectivity issues due to unavoidable side reactions and coke formation respectively[6].

On the other hand, CO_2 emission and global warming has become increasingly rough and severe over the past decades. CO_2 capture and CO_2 conversion related topics received worldwide attention, with great efforts and achievements from different fields such as photoreduction[7-9], electroreduction[10] and bio-mitigation[11]. In the field of propane dehydrogenation to produce propylene, CO_2 is also identified as a mild oxidant that can possibly open a more sustainable path with less environmental footprint than conventional propane dehydrogenation[12]. While the thermodynamics and technical barriers make PDH economically challenging, the introduction of CO_2 as a soft oxidant provides the following benefits: (1) the overall ODH reaction:

$$C_3H_8 + CO_2 \rightleftharpoons C_3H_6 + CO + H_2O$$

can be operated at milder than direct dehydrogenation reaction conditions; (2) CO_2-assissted ODH reaction can produce CO and H_2 (syngas) with suitable ratio, which can be directly incorporated in either downstream F-T synthesis[13] or tandem hydroformylation[14] ; (3) Coke formation can be suppressed either by reducing the formation of coke precursors[15] or by promoting the reverse Boudouard reaction[16, 17]:

$$C(s) + CO_2 \rightleftharpoons 2CO(g)$$

Despite these benefits, CO_2 is considered a "hard-to-activate" molecule due to its unique electronic properties and therefore, seeking catalytic strategies or developing novel materials that involve the activation of both C-H bonds of alkanes and CO_2 comprise a formidable challenge.

In our recent work[18], we shown that trivalent Fe ions successfully doped into ceria lattice with Ce:Fe atomic ratio = 10 (10Fe-CeO2) are very selective and stable catalyst for the CO_2

[a] Department of Chemical and Biochemical Engineering, Rutgers University, Piscataway NJ08854

assisted propane ODH. Building upon our previous efforts, in this work, surface dispersed CrO_x species were deposited over our prior stable support, i.e. 10Fe-CeO_2, with the intention to study their intrinsic kinetic behavior for CO_2-assisted propane dehydrogenation. CrO_x species on different types of metal and non-metal oxide supports have been reported in the open literature as promising materials with high catalytic activity towards selective propane dehydrogenation[19-22]. Herein, CrO_x/10Fe-CeO_2 with different Cr surface densities have been synthesized and evaluated physiochemically, spectroscopically and kinetically to understand its effects on propane dehydrogenation activity and propylene selectivity. A Langmuir-Hinshelwood kinetic model based on experimental results as well as literature data is also developed to investigate the intrinsic effect of Cr species.

Experimental

Synthesis of catalysts

$Ce(NO_3)_3{\cdot}6H_2O$ (99.99%), $Fe(NO_3)_3{\cdot}9H_2O$ (99.95%) and $Cr(NO_3)_3{\cdot}9H_2O$ (>99.99%) were purchased from Sigma Aldrich and used without further purification. The support, i.e. 10Fe-CeO_2 was synthesized via a co-precipitation method of aqueous Fe^{3+} and Ce^{3+} species where the entire synthesis is controlled by the crystalline growth mechanism proposed by Wang et al[23]. CrO_x/ Fe-CeO_2 catalysts were synthesized via incipient wetness impregnation of Cr on calcined 10Fe-CeO_2. We denote the catalysts as *n*Cr/10Fe-CeO_2, where *n* is the surface atomic density of Cr. Both 10Fe-CeO_2 and *n*Cr/10Fe-CeO_2 were calcined at 873K for 6 hours under air flow (50ml/min).

Catalyst characterization

Raman Spectroscopy

Raman spectra were collected with a Horiba Scientific LabRam HR Evolution Raman spectrometer cooled with a Synapse CCD detector (-70°C). The laser source used (532nm) was directed on the sample and focused by using a 50X long working distance objective. The power of the laser on the surface of the sample was controlled by using a neutral density filter at low level (5%) to avoid local overheating. In-situ Raman experiments were conducted in a Harrick Scientific high-temperature reaction chamber equipped with SiO_2 window. The nominal value of the temperature controller was calibrated with an independent thermocouple that was placed below the catalyst sample.

X-ray Powder Diffraction

XRD analysis was performed with a PANalytical Philips X'Pert X-Ray diffractometer to determine crystallinity and phase composition. The XRD instrument is equipped with a CuKα source at 45 kV and 40 mA and angular incidence 2θ between 20° and 90° with 0.05° step and 4.0 s/step. The phase composition was analysed by whole pattern fitting refinement analysis with relative error R% targeted below 15%. Silicon was used as an external standard reference to determine any possible peak shift.

Temperature-programmed reduction (H_2-TPR)

H_2-TPR experiments were conducted to investigate the redox properties of 10Fe-CeO_2 and *n*Cr/10Fe-CeO_2 catalysts. In each test, 50mg sample was loaded into a U-shape quartz reactor. The sample was pre-treated in air at 600°C for 1 hour to be fully dehydrated and fully oxidized, after which the sample was isolated in inert gas and cooled down to room temperature. TPR experiments were performed with 30sccm flow of 1%H_2/Ar at ramping rate of 10°C/min from 100°C to 650°C and then held at constant temperature for 20 minutes. The TPR pattern was evaluated by analyzing the water signal (m/z=18) collected with an in-line Mass Spectrometer (MKS Cirrus™ 3).

Kinetic Experiments

The propane ODH with CO2 reaction was conducted in a fix bed quartz tube reactor[18]. Propane (UHP, Praxair), CO2 (UHP, Airgas) and Nitrogen (UHP, Airgas) were mixed and co-fed at total flowrates in the range of 20-100mL/min using mass flow controllers (Alicat Scientific). Each catalyst was pre-heated under oxygen flow up to the desired reaction temperature and isolated in pure nitrogen to ensure no remaining oxygen prior and inside the reactor. The reactor outflow (product composition) was analysed with a MicroGC (Agilent, 490) equipped with a MS5A column (CH_4, H_2 and CO) and PPQ column (CO_2, C_2H_4, C_2H_6, C_3H_6, C_3H_8 and H_2O). In all kinetics experiments, the catalyst loading (typically 0.1g catalyst) and total flowrate mass were adjusted to achieve and low propane conversion (below 10%). The reaction temperature was varied in the range from 510 to 590°C. The effect of CO_2/C_3H_8 was also investigated. Propane conversion, product selectivity (on a propane base) and reaction rates were calculated according to:

$$X_{C_3H_8} = \frac{F_{in,C_3H_8} - F_{out,C_3H_8}}{F_{in,C_3H_8}} * 100\%$$

$$S_{C_xH_y} = \frac{\frac{x}{3} * F_{C_xH_y}}{F_{in,C_3H_8} - F_{out,C_3H_8}} * 100\%$$

$$Yield = X_{C_3H_8} * S_{C_3H_6}$$

$$-r_{C_3H_8} = \frac{dF_{C_3H_8}}{dw} \cong \frac{X_{C_3H_8}}{w/F_{in,C_3H_8}}$$

$$r_{C_3H_6} = \frac{dF_{C_3H_6}}{dw} \cong \frac{X_{C_3H_8} * S_{C_3H_6}}{w/F_{in,C_3H_8}}$$

Results and discussion

Physicochemical characterization and structural implications

Table 1 shows the BET results of the Fe-CeO_2 supports and Fe-CeO_2 supported CrO_x catalysts (see Figure S1 for the complete adsorption isotherms). The BET surface area features a monotonic decrease with increasing amount of Cr loading, which is consistent with supported Cr oxides reported in the literature[20, 24-26]. It is worth noting that nCr/Fe-CeO_2 has very low pore volume as compared to other materials[13, 20]. Small variation in BET measurements in conjunction with plausible

surface restructuring on the surface could lead to small fluctuations in the pore volume measurements, as observed in Table 1.

Table 1: *Summary of BET results of Cr/Fe-CeO$_2$ catalysts*

Catalyst	BET (m^2/g)	Pore width (nm)	Pore volume (cm^3/g)
10Fe-CeO_2	62	20	0.41
1Cr/10Fe-CeO_2	57	23	0.34
2Cr/10Fe-CeO_2	52	32	0.41
4Cr/10Fe-CeO_2	42	33	0.33

The X-ray diffractograms of the 10Fe-CeO_2 and *n*Cr/10Fe-CeO_2 with various Cr loadings shown in Figure 1 did not present any bulk crystalline oxide phases relevant to hematite and/or Cr_2O_3, suggesting that the support maintained its crystalline form while ensuring good Cr distribution. Below monolayer coverage, the impregnation of Cr species on the 10Fe-CeO_2 will result to the anchoring of amorphous surface species, usually acknowledged as tetrahedral Cr(VI)O_4 structure at fully oxidized and fully dehydrated conditions[27]. Depending on the surface density of Cr species, the unit structure can either remain as isolated monochromate or agglomerate to form polychromate species via Cr-O-Cr bonds.

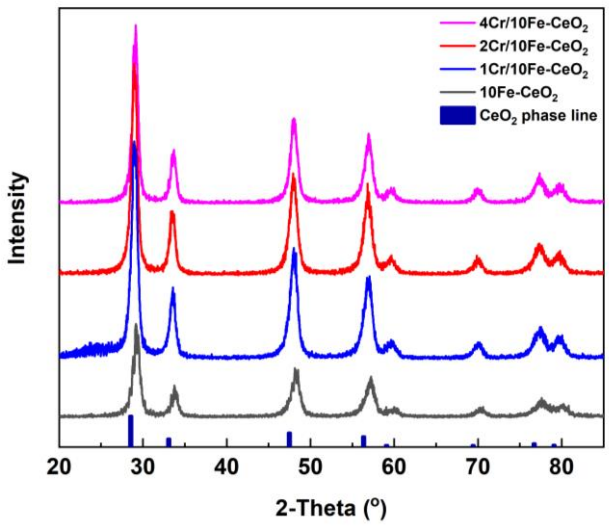

Figure 1: XRD patterns of the parent support, 10Fe-CeO2 as well as the *n*Cr/10Fe-CeO_2 catalysts with various Cr loadings

In

Figure 2a, we report the in-situ Raman spectra of all *n*Cr/10Fe-CeO_2 catalysts at fully oxidized and dehydrated conditions at 550°C. The most intense peak centred at ~450cm^{-1} corresponds to the F_{2g} vibrational mode of ceria support[28, 29]. The observed red shift of approximately 15cm^{-1} from the pure CeO_2 (usually observed at 465cm^{-1}) is related to the incorporation of Fe dopants inside ceria lattice[30-32] and depends on Fe/Ce atomic ratio[18]. The broad feature that appears at 590cm^{-1} is assigned as oxygen defect-related band[28] and the ratio of peak intensity I_{590}/I_{450} has been regarded as an indirect indicator of the relative abundance of oxygen vacancies.[33, 34] in CeO_2. Upon impregnation of chromium species, new peaks evolved at 539cm^{-1}, 837cm^{-1}, 998cm^{-1} and 1026cm^{-1}. The peaks at 998cm^{-1} and 1026cm^{-1} were assigned to isolated and polymeric Cr=O vibration respectively[20, 35, 36]. The broad band located around 837cm^{-1} is associated with either symmetric stretching of O-Cr-O[37, 38] or Cr-O-Cr[39] (845cm^{-1}) structure; however, there is a consensus that this peak is associated with the presence of polymeric species. Our Raman results are consistent with this assignment since the integrated peak area under 840cm^{-1} increases with increasing Cr loading. Besides, a sharp peak at 539cm^{-1} over 4Cr/10Fe-CeO_2 oxide pertains to A_{1g} symmetric vibrational mode of Cr_2O_3[39]. In addition, the normalized peak intensity for the F_{2g} vibration decreases significantly over 4Cr/10Fe-CeO_2 oxide. Even though the XRD data revealed no crystalline phases of chromium oxide, the Raman results suggest the formation of chromium crystalline phases (nano-sized) at high Cr surface density (i.e. 4Cr/nm^2) indicating the overreach of monolayer coverage on the 10Fe-CeO_2 oxide surface. Relevant TEM images (Figure 2b,c) show changes in the textural properties after impregnation of Cr oxides. While the original Fe-CeO_2 exhibits a well-defined hexagonal, the addition of Cr oxides modified the external surface turning into spherical-like agglomerates.

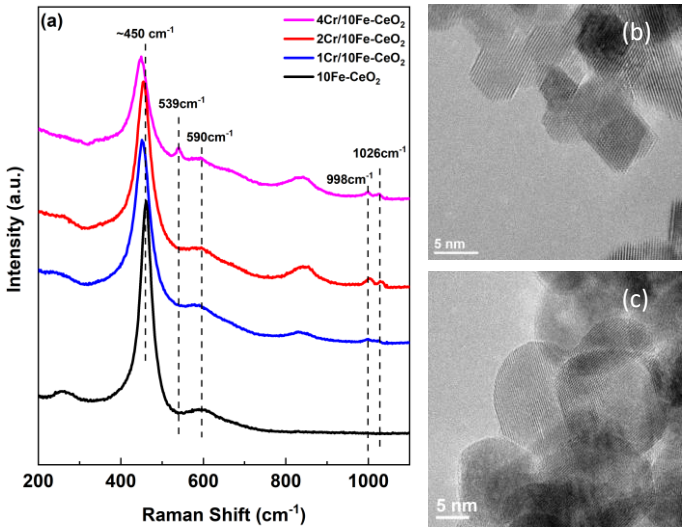

Figure 2: (a) In-situ Raman spectra of Cr-10Fe-CeO_2 catalysts with different Cr loading at fully oxidized and dehydrated conditions. (b) TEM imaging of 10Fe-CeO_2 sample. (c) TEM imaging of 2Cr/10Fe-CeO_2 oxide.

Reducibility and Active Surface Oxygen Sites

H_2-TPR experiments were conducted to reveal the difference in the redox properties of catalysts due to the change of the available surface oxygen species with different bonding and electronic environment. All TPR experiments were performed up to a maximum temperature of 650 °C to ensure that the mesoporous structure of the support will remain while avoiding

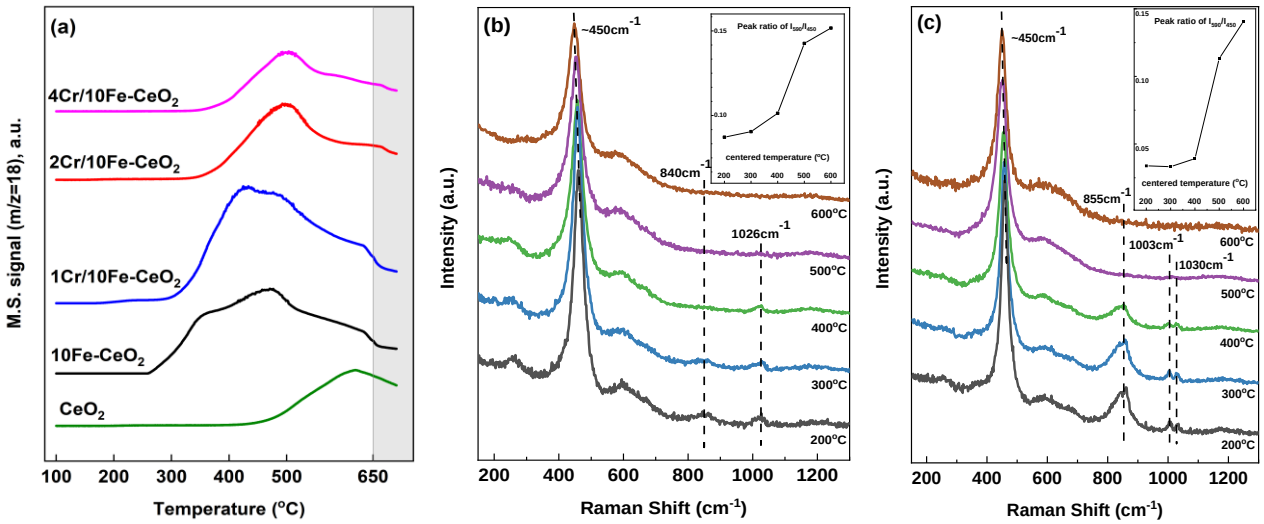

Figure 3: (a) H2-TPR profile of pure CeO_2, 10Fe-CeO_2, 1Cr/10Fe-CeO_2, 2Cr/10Fe-CeO_2 and 4Cr/10Fe-CeO_2 oxides, (b)In-situ Raman spectra coupled with H_2- TPR experiments of 1Cr/10Fe-CeO_2. (c) In-situ Raman spectra coupled with H_2- TPR experiments of 2Cr/10Fe-CeO_2. Insert: peak ratio of I_{590}/I_{450} of 1Cr/10Fe-CeO_2 and 2Cr/10Fe-CeO_2 during H_2-TPR at different temperature stage.

potential phase separation of cerianite and hematite[18]. In Figure 3a, H_2-TPR data for representative catalysts as well as pure CeO_2 (for comparison) are presented. Bare CeO_2 shows a broad peak centred at 550 to 600°C, which is attributed to the reduction of reactive surface oxygen species[40, 41]. Since the total reduction of CeO_2 to Ce_2O_3 is only expected in the temperature range of 800 to 900°C, the broad reduction band suggests the creation of oxygen defects and exposure of Ce^{3+} on the surface[40, 42, 43]. This argument is also supported by our in-situ Raman H_2-TPR results in Figures 3b and c. The band at 245cm^{-1} representing the transverse acoustic mode of surface oxygen[44], is gradually decreased during H_2-TPR. In addition, we observe an increase in the relative peak intensity ratio (~590 cm^{-1} / 450 cm^{-1}), that indicates an increase in the defect domains (oxygen vacancies)[28]. Upon doping of Fe into cerium oxide lattice, the main peak shifted to around 360°C, indicating the enhanced surface reducibility as compared to bare CeO_2[45]. Despite the presence of Fe ion in the bulk phase, the early TPR-H_2 feature is not due to the reduction of crystalline Fe_2O_3 since all relevant characterization results, i.e., the XRD and Raman, as well as prior extensive characterization of our support[18], confirm the absence of separated crystalline iron oxide phase. Thus, the feature at around 360°C should be attributed to the weakening of the lattice bond between metal ions and O due to hetero-atom doping which is strongly supported by the shift in the diffractogram. As stated in our previous work[18], the surface oxygen to Fe-CeO_2 oxide should be predominately involved in two types of structures: Fe-rich sites (Fe-O-Ce) and Fe-free sites (Ce-O-Ce). A new peak appeared at around 470°C, which has been previously assigned as adsorbed peroxide (O_2^{2-}) or superoxide (O_2^-) species on oxygen vacancies[28] due to long-time calcination. However, we cannot exclude the possibility the addition of Fe ions into the CeO_2 lattice structure may also weaken the bond strength of *Metal*-O leading to an increase in the apparent reducibility of oxygen species at the surface. The impregnation of CrO_x sites reconstructs the surface through the formation of Cr-O-support bridging bond in order to balance its degree of coordinative unsaturation[47], during which the original surface oxygen sites may be consumed or diffuse into subatomic layers. As a result, those oxygen sites are no longer exposed or accessible to H_2 in the gas phase[48]. Particularly, at high Cr loadings approaching monolayer coverage (2Cr/10Fe-CeO_2 and 4Cr/10Fe-CeO_2) when polymeric CrO_x species dominate the catalyst surface, we observe a decrease in the total area of H_2 consumed. The original Fe-rich sites disappeared from TPR signal and a broad band starting from

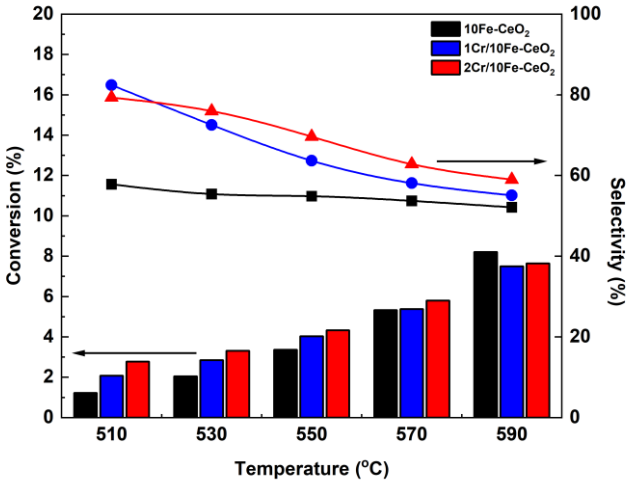

Figure 4: Catalytic performance of 10Fe-CeO_2 and Cr supported 10Fe-CeO_2 catalysts under intrinsic kinetic regime. Exp. parameters: 510 to 590°C, 1atm, 100mL/min total flow with 5% propane and 5% carbon dioxide, 100mg catalyst loading.

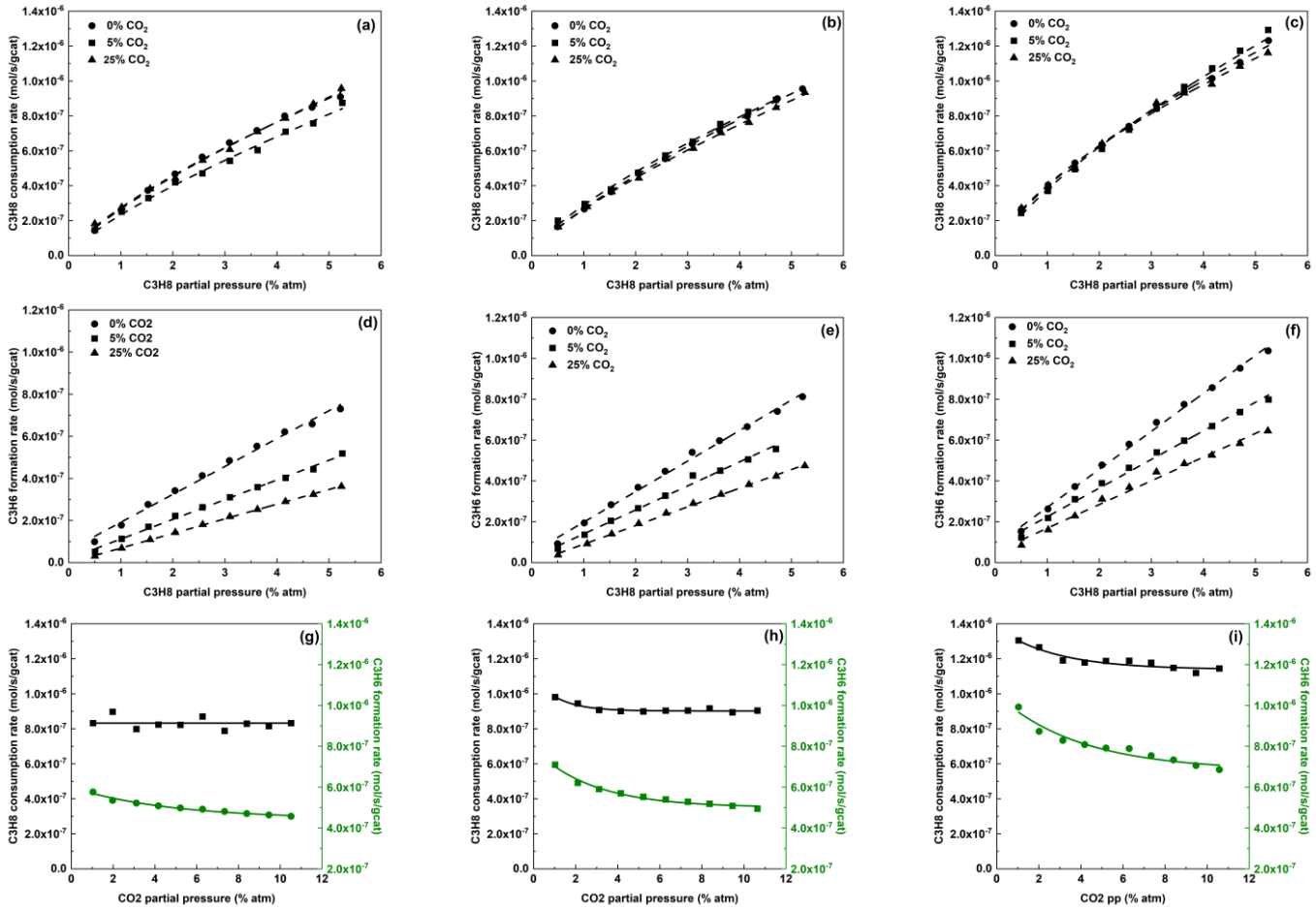

Figure 5: Kinetic behaviour of 10Fe-CeO_2 (a,d,g), 1Cr/10Fe-CeO_2 (b,e,h) and 2Cr/10Fe-CeO_2 (c,f,i) catalysts with respect to changes in the partial pressure of propane and CO_2. Reactivity is investigated at 550 °C. (a,b,c) Propane consumption rate, (d,e,f) propylene formation rate, (g,h,i)propane and propylene reaction rates as a function of CO_2 partial pressure.

~400°C and centred at ~500°C indicates the formation of new oxidation sites. Interestingly, the Raman data revealed that the band at around 845cm^{-1} disappeared prior to that at ~1000-1030cm^{-1} pointing that the broad feature around 430°C corresponds to the Cr-O bridging bonds while the ~500°C to the Cr=O terminal bonds.

Kinetic Studies

Effect of temperature

The effect of temperature on the performance of all catalysts was evaluated in the 510-590°C range. The total flow and mass of catalyst were appropriately selected to ensure that all measurements performed at the kinetic regime. Figure 4 shows the temperature dependent propane conversion and propylene selectivity for the 10Fe-CeO_2, 1Cr/10Fe-CeO_2 and 2Cr/10Fe-CeO_2. The overall behaviour is consistent with an improved catalytic performance (propylene yield) upon addition of chromium sites on the surface of 10Fe-CeO_2. Propylene selectivity decreases with increasing temperature for the Cr-based catalysts while, interestingly, it remains almost constant for the bare support. This behaviour is indicative that the supported CrO_x sites provide unique surface properties that unlock selective dehydrogenation pathways which are kinetically more favourable at low temperatures. This is also consistent with the H_2-TPR and Raman measurements discussed above where the presence of Cr-O and Cr=O can be regarded as surface oxygen sites for propane adsorption. However, after dehydrogenation, oxygen defects/vacancies have to be replenished by CO_2 thus next we evaluate the effect of CO_2 on intrinsic kinetics.

Effect of reactant partial pressure on rates

The effects of partial pressure as well as the ratio of propane to CO_2 on reactivity were studied at 550°C under differential conditions. Relevant results are summarized in Figure 5. Upon increasing CO_2, the rate of propane consumption appears to be unaffected (Figure 5a-c) underscoring that CO_2 is not involved in the rate controlling step of propane activation, especially under low partial pressure conditions where competitive adsorption will not play a significant role. In the case of the bare support (Figure 5g), the rate of propane consumption remains constant upon increasing the partial pressure of CO_2 in the reaction stream while for CrO_x based catalysts, propane consumption slightly decreased with a small increase of CO_2 and then remain constant (Figure 5h-i). On the other hand, the rate of propylene formation decreases monotonically (Figure 5d-f) with increasing CO_2. This decrease is ascribed to a shift from

direct dehydrogenation to the thermodynamically favorable dry reforming at high CO_2/C_3H_8 conditions; the higher the CO_2 in the feed, the larger the dry reforming (DRF) contribution. In general, the addition of chromium species increases both the intrinsic rate of propane consumption and propylene formation highlighting the positive impact of CrO_x on productivity. The beneficial effect of CO2 in the propylene formation has been underscored in the literature[49, 50]. However, it is worth mentioning that the effect of CO_2 in the overall propane conversion as well as propylene formation depends on multiple factors that may include the nature of active sites present which in turn may govern the relative contribution of simultaneous reactions such as DH vs. reforming[51] and/or DH/ODH[52]. Moreover, CO_2 may participate directly in reoxidizing reduced metal oxide centers thus its conversion competing the reverse water gas shift reaction.

The rate of propane consumption can be represented by the following power-law kinetic expression

$$-r_{C_3H_8} = k_{app} P_{C_3H_8}{}^{\alpha} P_{CO_2}{}^{\beta}$$

Table 2 Summary of apparent reaction orders of propane consumption rate and propane overall activation energy

Catalyst	C_3H_8 reaction order (α)	CO_2 reaction order (β)
10Fe-CeO_2	0.71	-0.06
1Cr/10Fe-CeO_2	0.74	-0.03
2Cr/10Fe-CeO_2	0.64	-0.02

, where α and β are the apparent reaction orders for propane and CO_2 respectively. Numerical values of the apparent orders for propane conversion are given in Table 2 and relevant analysis in Figure S4. It is shown that the apparent propane reaction order for 10Fe-CeO_2, 1Cr/10Fe-CeO_2 and 2Cr/10Fe-CeO_2 are 0.71, 0.74 and 0.64, respectively. The actual apparent order is expected between 1 and 0.33 depending on the relative contribution of PDH and DRF. Values reported in this study are in agreement with a recent kinetic study by Shishido et al.[53] where reaction orders of partial pressure of propane over Cr/SiO_2 and Cr/Al_2O_3 catalysts were found to be 0.65 and 0.59, respectively. It is also shown that propane conversion has almost zeroth order dependence on CO_2. The kinetic data of this study were collected at a low partial pressure regime (from 0.5% to 5%), where competitive adsorption of propane and CO_2 may not be taken into account. According to Chen et al.[51], competitive adsorption and reduction of C_3H_8 reaction rates occurs severely when CO_2 in the feed exceeds certain partial pressure threshold depending on the type of active sites and support surface.

Mechanistic Implications and Langmuir-Hinshelwood model

The characterization and kinetic results discussed in the previous sections set the foundation to propose the following steady-state kinetic model that assumes: (a) Two types of active sites (identified from previous literature reports[18, 45, 54, 55]), i.e. surface active oxygen sites (S_1) and oxygen vacancies (S_2). (b) No migrations of adsorbed intermediates between S_1 and S_2 sites. (c) single site adsorption. (d) Langmuir-Hinshelwood Hougen-Watson (LHHW) surface reaction mechanism was applied to describe the overall reaction network comprised by PDH, DRF and RWGS assuming a primary rate-limiting step (p-rds) and two secondary rate-limiting steps (s-rds). Based on these assumptions, the kinetics observed in this work can be rationalized using the following 14 elementary steps:

s1: $C_3H_8(g) + 2S_1 \rightleftharpoons C_3H_7\_S_1 + H\_S_1$

s2: $C_3H_7\_S_1 \rightleftharpoons C_3H_6(g) + H\_S_1$

s3: $2H\_S_1 \rightleftharpoons H_2(g) + 2S_1$

s4: $CO_2(g) + S_2 \rightleftharpoons CO(g) + S_1$

s5: $CO_2(g) + S_2 + H\_S_1 \rightleftharpoons COOH\_S_2 + S_1$

s6: $COOH\_S_2 \rightleftharpoons CO(g) + HO\_S_2$

s7: $2HO\_S_2 \rightleftharpoons H_2O(g) + S_1 + S_2$

s8: $C_3H_7\_S_1 + S_1 \rightleftharpoons CH_3CH\_S_1 + CH_3\_S_1$

s9: $CH_3CH\_S_1 + S_1 \rightleftharpoons CH_3\_S_1 + CH\_S_1$

s10: $CH_3\_S_1 \rightleftharpoons CH_3O\_S_2$

s11: $CH\_S_1 \rightleftharpoons CHO\_S_2$

s12: $CH_3O\_S_2 + S_1 \rightleftharpoons CH_2O\_S_2 + H\_S_1$

s13: $CH_2O\_S_2 + S_1 \rightleftharpoons CHO\_S_2 + H\_S_1$

s14: $CHO\_S_2 + S_1 \rightleftharpoons CO(g) + H\_S_1 + S_2$

In this proposed reaction scheme, the reactant molecules, C_3H_8 and CO_2, are independently adsorbed and activated on surface oxygen sites and oxygen vacancies respectively. The formed $C_3H_7\_S_1$, is hypothesized to further evolve via two distinct reaction paths: i) a secondary dehydrogenation to result the desired olefin via PDH and/or ii) C-C scissoring. For the latter case, the light hydrocarbon species can further react through two competitive paths that i) upon the participation of oxygen sites will lead to dry reforming products or ii) will produce coke precursors and migrate to form coke and block certain active sites. It has been suggested that small hydrocarbon species may further decompose to atomic carbon and then oxidized to form CO[56, 57]. Recently, however, by means of computational efforts, it was shown that low hydrocarbon species (CH_x) can be involved in the surface elementary reaction with O^* or -OH to form CH_xO[58-60]. In this work, the latter is considered more realistic since the Fe-CeO_2 oxides were shown to have reactive surface oxygen site that could readily oxidizing low hydrocarbon intermediates before they completely turned to atomic carbon[18]. In addition, our previous work showed minimum coke formation over 10Fe-CeO_2 surface, which further reduces the possibility of atomic carbon formation, especially at low propane conversion that this modelled is developed. On the other hand, CO_2 is adsorbed independently on the surface. The activation of CO_2 is fulfilled via two possible approaches: direct dissociation to generate adsorbed CO and O^*[18, 55, 61, 62] or combined with adsorbed hydrogen atoms (mostly generated via propane C-H activation step) and form carboxyl intermediates(-COOH), which further decompose to CO and hydroxyl group(-OH). The latter is also known as the associative mechanism of reverse water-gas shift reaction[62-65].

Assuming s14 as primary rate-limiting step, s1 and s4 as secondary rate-limiting step, the overall PDH, DRF and RWGS rates were expressed as:

$$r_{DH} = \frac{k_{DH}\left(P_{C_3H_8}P_{H_2}^{-1/2} - \frac{P_{C_3H_6}P_{H_2}^{1/2}}{K_{DH}}\right)}{\left[1 + K_2^{-1}P_{C_3H_6}\left(K_{H_2}P_{H_2}\right)^{0.5} + \left(K_{H_2}P_{H_2}\right)^{0.5}\right]}$$

$$r_{RWGS} = \frac{k_{RWGS}\left(P_{CO_2}^2P_{CO}^{-2}P_{H_2} - \frac{P_{H_2O}}{K_{RWGS}}\right)}{\left(1 + K_5P_{CO_2}\left(K_{H_2}P_{H_2}\right)^{0.5}\left(1 + \frac{K_5}{P_{CO}}\right) + \frac{K_{CHO}P_{C_3H_6}{}^{1/3}P_{CO_2}}{P_{CO}\left(P_{H_2}\right)^{\frac{1}{2}}}\right)^2}$$

$$r_{DRF} = \frac{k_{DRF}\left[P_{C_3H_8}^{1/3}P_{CO_2}P_{CO}^{-1}P_{H_2}^{-5/6} - \frac{P_{CO}P_{H_2}{}^{1/2}}{K_{DRF}}\right]\left[1 + K_2^{-1}P_{C_3H_6}\left(K_{H_2}P_{H_2}\right)^{0.5} + \left(K_{H_2}P_{H_2}\right)^{0.5}\right]^{-1}}{1 + K_5P_{CO_2}\left(K_{H_2}P_{H_2}\right)^{0.5}\left(1 + \frac{K_5}{P_{CO}}\right) + \frac{K_{CHO}P_{C_3H_6}{}^{1/3}P_{CO_2}}{P_{CO}\left(P_{H_2}\right)^{\frac{1}{2}}}}$$

Details of the regressed kinetic parameters are summarized in Table 3 and a parity plot of predicted rates with respect to observed rates for 10Fe-CeO_2, 1Cr/10Fe-CeO_2 and 2Cr/10Fe-CeO_2 are also shown in Figure 6. Activation energies of propane dehydrogenation and dry reforming over similar reported catalyst system have been summarized in Table 3 for comparison. In Figure S2, we show data for the propane conversion vs. W/F. We show that at low flow rates, i.e., below 50ml/min, some deviation from the linear behavior is observed that may point to small transport limitations. It is worth mentioning here that all data that have been used for the kinetic analysis and regression pertain to flow rates of 100ml/min thus ensuring no transport limitations. As seen from Table 3, the activation energy for propane CO_2-assisted propane dehydrogenation is 109 kJ/mol for the bare support. Upon impregnating Cr on the Fe-CeO_2 surface, the activation energy was decreased drastically down to 44.4 and 28.4kJ/mol, depending on the Cr surface density. The differences in activation energy implies that as compared to the bare support surface, propane molecules are preferably activated on the Cr active sites. On the other hand, the activation energies of propane dry reforming are less affected by supported Cr species, indicating that dry reforming pathway is contributed mostly from the Fe-CeO_2 oxide support. CrO_x active sites are more selective towards propane dehydrogenation, which is also consistent with high selectivity reported in most Cr-related catalyst (Cr/Silica[20, 25, 73], Cr/SBA[74, 75], Cr/Al_2O_3[75], etc.) in the CO_2-assisted propane dehydrogenation.

Table 3: Summary of reaction rate constants and reactants adsorption equilibrium constants regressed by the steady-state model and activation energies reported from literature obtained by experimental and computational works.

	PDH		DRF	
Catalyst (This work)	**k_0 (at 550°C)**	**Ea (kJ/mol)**	**k_0 (at 550°C)**	**Ea (kJ/mol)**
10Fe-CeO_2	$1.49*10^{-5}$ (± $9.6*10^{-7}$)	109 (± 2.4)	$2.57*10^{-5}$ (± $9.4*10^{-6}$)	140 (± 8.4)
1Cr/10Fe-CeO_2	$1.97*10^{-5}$ (± $1.5*10^{-6}$)	44.4 (± 7.1)	$3.6*10^{-5}$ (± $1.3*10^{-6}$)	120 (± 11)
2Cr/10Fe-CeO_2	$2.68*10^{-5}$ (± $2.4*10^{-6}$)	28.4 (± 4.1)	$4.15*10^{-5}$ (± $1.5*10^{-6}$)	115 (± 17)

Literature reported activation energies for propane direct dehydrogenation (PDH) and dry reforming (DRF) for different catalytic systems and methods used.

Catalyst	**PDH, Ea (kJ/mol)**		**Catalyst**	**DRF, Ea (kJ/mol)**	
Pt-Sn/CeO_2[66]	41.5	DFT	Co_3Pt_1/CeO_2[67]	126	Arrhenius plot
Cr/Al_2O_3[68]	35.5	Model regression	Co-Ni/Al_2O_3[69]	92.3	Arrhenius plot
NbO_x/CeO_2[70]	45.2-69.2	Arrhenius plot	Ni_3Pt/CeO_2[51]	119	DFT
Cr/$SiAlO_x$[71]	up to 40	Enthalpy of activation	Ni/Mg(Al)O[72]	93	Arrhenius plot

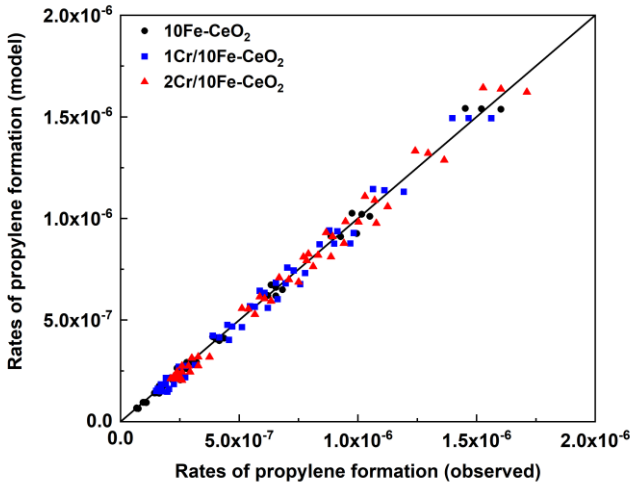

Figure 6: Parity plot of predicted rates versus experimental calculated rates.

Figure 6 compares the results of the kinetic model with all catalytic data reported previously for the rate of propylene formation. The model predictions for the propane consumption are also reported in Figure S5 of the supporting information. The proposed model of this work predicts well both propane consumption and propylene production rates. It should be noted though that the developed kinetic model should be used for predicting the catalytic behavior solely within the reaction conditions of this study and especially at low to moderate CO_2 partial pressure. As stated previously, competitive adsorption of propane and CO_2 needs to be considered at high partial pressure regime (above 15%), which may significantly alter the adsorption constants of both propane and CO_2. Besides, at elevated temperatures, e.g. approaching 800°C, the net rate of C-C cracking and coke formation[76] will be boosted and lead to a deficiency in total carbon and hydrogen balance. In such case,

an additional deactivation model will be required in the future to better describe the extended reaction network.

Conclusions

*n*Cr/10Fe-CeO_2 catalysts with different Cr loadings were synthesized via a two-step approach. Raman spectroscopy was utilized to investigate the molecular structure of the surface species confirming the presence of monomeric and polymeric CrO_x sites. The CO_2-assissted propane dehydrogenation reaction was performed over the bare 10Fe-CeO_2 support as well as all supported chromium catalysts. Our catalytic data in the intrinsic kinetic regime revealed that Cr-supported catalysts provided improved initial propane conversion and propylene selectivity at low temperatures. Combining the data from the H_2-TPR, Raman and kinetics together with the proposed model, we show that although DH will be promoted due to CrO_x addition, the enhanced reducibility of such sites lead to an apparent increase of DRF pathway at high temperatures. The overall consumption rate of propane was mainly dependent on the partial pressure of propane with an apparent reaction order ~0.7, whereas CO_2 partial pressure significantly hampered the overall propylene selectivity. A steady-state kinetic model was developed to account for the major reaction pathways, that is PDH, DRF and RWGS, occurring simultaneously at the temperature range of this work. Reaction rate constants and reactants adsorption constant were regressed from kinetic data, from which it was observed that the addition of CrO_x decreases the activation energy of PDH by 60-75% as compared to the bare support; the effect of CrO_x on the activation energy of DRF was much smaller.

Conflicts of interest

There are no conflicts to declare.

Acknowledgements

This material is based upon work supported in part by Rutgers, The State University of New Jersey, and the National Science Foundation Award #1751683. The authors would like to thank Prof. T. Asefa for helping with the BET measurements and porosity analysis, Prof. W. Zheng from University of Delaware for TEM analysis and discussion, and Prof. F. Celik for discussion in kinetic analysis.

References

1. E. E. Stangland, *Annu Rev Chem Biomol Eng*, 2018, **9**, 341-364.
2. Y. Chen and J. Xu, *Journal of Cleaner Production*, 2019, **229**, 399-411.
3. K. Aruga, *Journal of Unconventional Oil and Gas Resources*, 2016, **14**, 1-5.
4. S. Chen, X. Chang, G. Sun, T. Zhang, Y. Xu, Y. Wang, C. Pei and J. Gong, *Chem Soc Rev*, 2021, **50**, 3315-3354.
5. S. Dong, N. R. Altvater, L. O. Mark and I. Hermans, *Applied Catalysis A: General*, 2021, **617**.
6. F. Cavani, N. Ballarini and A. Cericola, *Catalysis Today*, 2007, **127**, 113-131.
7. S. Gong, G. Zhu, R. Wang, F. Rao, X. Shi, J. Gao, Y. Huang, C. He and M. Hojamberdiev, *Applied Catalysis B: Environmental*, 2021, **297**.
8. S. Mazzanti, S. Cao, K. ten Brummelhuis, A. Völkel, J. Khamrai, D. I. Sharapa, S. Youk, T. Heil, N. V. Tarakina, V. Strauss, I. Ghosh, B. König, M. Oschatz, M. Antonietti and A. Savateev, *Applied Catalysis B: Environmental*, 2021, **285**.
9. Y. Liu, C. Miao, P. Yang, Y. He, J. Feng and D. Li, *Applied Catalysis B: Environmental*, 2019, **244**, 919-930.
10. P. Lu, Y. Yang, J. Yao, M. Wang, S. Dipazir, M. Yuan, J. Zhang, X. Wang, Z. Xie and G. Zhang, *Applied Catalysis B: Environmental*, 2019, **241**, 113-119.
11. P. C. Sahoo, R. Kumar, M. Kumar, S. Kumar Puri and S. S. V. Ramakumar, *International Journal of Greenhouse Gas Control*, 2019, **90**.
12. M. A. Atanga, F. Rezaei, A. Jawad, M. Fitch and A. A. Rownaghi, *Applied Catalysis B: Environmental*, 2018, **220**, 429-445.
13. P. Michorczyk, P. Pietrzyk and J. Ogonowski, *Microporous and Mesoporous Materials*, 2012, **161**, 56-66.
14. Z. H. Xie, H. Y. Guo, E. R. Huang, Z. T. Mao, X. B. Chen, P. Liu and J. G. Chen, *Acs Catal*, 2022, DOI: 10.1021/acscatal.2c01700, 8279-8290.
15. F. Solymosi, P. Tolmacsov and K. Kedves, *Journal of Catalysis*, 2003, **216**, 377-385.
16. B. Xu, B. Zheng, W. Hua, Y. Yue and Z. Gao, *Journal of Catalysis*, 2006, **239**, 470-477.
17. B. Xu, B. Zheng, W. Hua, Y. Yue and Z. Gao, *Studies in Surface Science and Catalysis*, 2007, **170**, 1072-1079.
18. H. Wang and G. Tsilomelekis, *Catalysis Science & Technology*, 2020, DOI: 10.1039/d0cy00586j.
19. K. Takehira, Y. Ohishi, T. Shishido, T. Kawabata, K. Takaki, Q. Zhang and Y. Wang, *Journal of Catalysis*, 2004, **224**, 404-416.
20. J. Baek, H. J. Yun, D. Yun, Y. Choi and J. Yi, *Acs Catal*, 2012, **2**, 1893-1903.
21. J. F. S. de Oliveira, D. P. Volanti, J. M. C. Bueno and A. P. Ferreira, *Applied Catalysis A: General*, 2018, **558**, 55-66.
22. X. Zhang, Y. Yue and Z. Gao, *Catalysis Letters*, 2002, **83**, 19-25.
23. Z. Wang, Y. Xin, Z. Zhang, Q. Li, Y. Zhang and L. Zhou, *Chemical Engineering Journal*, 2011, **178**, 436-442.
24. P. Kuśtrowski, P. Michorczyk, L. Chmielarz, Z. Piwowarska, B. Dudek, J. Ogonowski and R. Dziembaj, *Thermochimica Acta*, 2008, **471**, 26-32.
25. D. Yun, J. Baek, Y. Choi, W. Kim, H. J. Lee and J. Yi, *ChemCatChem*, 2012, **4**, 1952-1959.
26. M. A. Botavina, Y. A. Agafonov, N. A. Gaidai, E. Groppo, V. Cortés Corberán, A. L. Lapidus and G. Martra, *Catalysis Science & Technology*, 2016, **6**, 840-850.
27. M. Cherian, M. S. Rao, A. M. Hirt, I. E. Wachs and G. Deo, *Journal of Catalysis*, 2002, **211**, 482-495.
28. Z. Wu, A. J. Rondinone, I. N. Ivanov and S. H. Overbury, *The Journal of Physical Chemistry C*, 2011, **115**, 25368-25378.

29. B. Penkala, D. Aubert, H. Kaper, C. Tardivat, K. Conder and W. Paulus, *Catalysis Science & Technology*, 2015, **5**, 4839-4848.
30. S. Chong, G. Zhang, N. Zhang, Y. Liu, J. Zhu, J. Huang and S. Fang, *Untrasonics Sonochemistry*, 2016, **32**, 231-240.
31. K. Li, M. Haneda, P. Ning, H. Wang and M. Ozawa, *Applied Surface Science*, 2014, **289**, 378-383.
32. O. H. Laguna, M. A. Centeno, M. Boutonnet and J. A. Odriozola, *Applied Catalysis B: Environmental*, 2011, **106**, 621-629.
33. M.-F. Luo, Z.-L. Yan, L.-Y. Jin and M. He, *J. Phys. Chem. B*, 2006, **110**, 13068-13071.
34. M. Ridwan, R. Tamarany, J. Han, S. W. Nam, H. C. Ham, J. Y. Kim, S. H. Choi, S. C. Jang and C. W. Yoon, *RSC Advances*, 2015, **5**, 89478-89481.
35. E. L. Lee and I. E. Wachs, *J. Phys. Chem. C*, 2007, **111**, 14410-14425.
36. S. D. Yim and I.-S. Nam, *Journal of Catalysis*, 2004, **221**, 601-611.
37. T. A. Bugrova, V. V. Dutov, V. A. Svetlichnyi, V. Cortés Corberán and G. V. Mamontov, *Catalysis Today*, 2019, **333**, 71-80.
38. D. S. Kim and I. E. Wachs, *J. Catal.*, 1993, **142**, 166-171.
39. H. Xie, H. Wang, Q. Geng, Z. Xing, W. Wang, J. Chen, L. Ji, L. Chang, Z. Wang and J. Mao, *Inorg Chem*, 2019, **58**, 5423-5427.
40. Z. Zhang, D. Han, S. Wei and Y. Zhang, *Journal of Catalysis*, 2010, **276**, 16-23.
41. Z. Lendzion-Bielun, M. M. Bettahar and S. Monteverdi, *Catalysis Communications*, 2010, **11**, 1137-1142.
42. Tana, M. Zhang, J. Li, H. Li, Y. Li and W. Shen, *Catalysis Today*, 2009, **148**, 179-183.
43. S. Watanabe, X. Ma and C. Song, *J. Phys. Chem. C*, 2009, **113**, 14249-14257.
44. Z. Wu, M. Li, J. Howe, H. M. Meyer, 3rd and S. H. Overbury, *Langmuir*, 2010, **26**, 16595-16606.
45. H.-X. Fan, J. Feng and W.-Y. Li, *Applied Surface Science*, 2019, **486**, 411-419.
46. C. Beasley, M. K. Gnanamani, H. H. Hamdeh, M. Martinelli and B. H. Davis, *Catalysis Letters*, 2018, **148**, 1920-1928.
47. B. M. Weckhuysen, I. E. Wachs and R. A. Schoonheydt, *Chem Rev*, 1996, **96**, 3327-3349.
48. X. Li, S. Wei, Z. Zhang, Y. Zhang, Z. Wang, Q. Su and X. Gao, *Catalysis Today*, 2011, **175**, 112-116.
49. K. Bian, G. Zhang, J. Zhu, X. Wang, M. Wang, F. Lou, Y. Liu, C. Song and X. Guo, *Acs Catal*, 2022, **12**, 6559-6569.
50. Y. Ren, F. Zhang, W. Hua, Y. Yue and Z. Gao, *Catalysis Today*, 2009, **148**, 316-322.
51. E. Gomez, S. Kattel, B. Yan, S. Yao, P. Liu and J. G. Chen, *Nat Commun*, 2018, **9**, 1398.
52. T. D. Nguyen, W. Zheng, F. E. Celik and G. Tsilomelekis, *Catalysis Science & Technology*, 2021, **11**, 5791-5801.
53. T. Shishido, K. Shimamura, K. Teramura and T. Tanaka, *Catalysis Today*, 2012, **185**, 151-156.
54. A. Hezam, K. Namratha, Q. A. Drmosh, D. Ponnamma, J. Wang, S. Prasad, M. Ahamed, C. Cheng and K. Byrappa, *ACS Applied Nano Materials*, 2019, **3**, 138-148.
55. E. Nowicka, C. Reece, S. M. Althahban, K. M. H. Mohammed, S. A. Kondrat, D. J. Morgan, Q. He, D. J. Willock, S. Golunski, C. J. Kiely and G. J. Hutchings, *Acs Catal*, 2018, **8**, 3454-3468.
56. A. Siahvashi and A. A. Adesina, *Industrial & Engineering Chemistry Research*, 2013, **52**, 15377-15386.
57. S. Chen, J. Zaffran and B. Yang, *Applied Catalysis B: Environmental*, 2020, **270**.
58. A. Hook, T. P. Nuber and F. E. Celik, *Industrial & Engineering Chemistry Research*, 2018, **57**, 8131-8143.
59. M. Jørgensen and H. Grönbeck, *Acs Catal*, 2016, **6**, 6730-6738.
60. M. Van den Bossche and H. Gronbeck, *J Am Chem Soc*, 2015, **137**, 12035-12044.
61. X. Zhang, X. Zhu, L. Lin, S. Yao, M. Zhang, X. Liu, X. Wang, Y.-W. Li, C. Shi and D. Ma, *Acs Catal*, 2016, **7**, 912-918.
62. A. Hook and F. E. Celik, *Industrial & Engineering Chemistry Research*, 2018, **57**, 6830-6841.
63. L. Huang, B. Han, Q. Zhang, M. Fan and H. Cheng, *The Journal of Physical Chemistry C*, 2015, **119**, 28934-28945.
64. M. Zhu and I. E. Wachs, *Acs Catal*, 2016, **6**, 2827-2830.
65. X. Su, X. Yang, B. Zhao and Y. Huang, *Journal of Energy Chemistry*, 2017, **26**, 854-867.
66. H. Xiong, S. Lin, J. Goetze, P. Pletcher, H. Guo, L. Kovarik, K. Artyushkova, B. M. Weckhuysen and A. K. Datye, *Angew Chem Int Ed Engl*, 2017, **56**, 8986-8991.
67. E. Gomez, Z. Xie and J. G. Chen, *AIChE Journal*, 2019, **65**.
68. J. Gascón, C. Téllez, J. Herguido and M. Menéndez, *Applied Catalysis A: General*, 2003, **248**, 105-116.
69. F. M. Althenayan, S. Yei Foo, E. M. Kennedy, B. Z. Dlugogorski and A. A. Adesina, *Chemical Engineering Science*, 2010, **65**, 66-73.
70. R. You, X. Zhang, L. Luo, Y. Pan, H. Pan, J. Yang, L. Wu, X. Zheng, Y. Jin and W. Huang, *Journal of Catalysis*, 2017, **348**, 189-199.
71. M. F. Delley, M.-C. Silaghi, F. Nuñez-Zarur, K. V. Kovtunov, O. G. Salnikov, D. P. Estes, I. V. Koptyug, A. Comas-Vives and C. Copéret, *Organometallics*, 2016, **36**, 234-244.
72. A. Olafsen, A. Slagtern, I. Dahl, U. Olsbye, Y. Schuurman and C. Mirodatos, *Journal of Catalysis*, 2005, **229**, 163-175.
73. P. Michorczyk, J. Ogonowski and K. Zeńczak, *Journal of Molecular Catalysis A: Chemical*, 2011, **349**, 1-12.
74. P. Michorczyk, J. Ogonowski and M. Niemczyk, *Applied Catalysis A: General*, 2010, **374**, 142-149.
75. M. Santhoshkumar, N. Hammer, M. Ronning, A. Holmen, D. Chen, J. Walmsley and G. Oye, *Journal of Catalysis*, 2009, **261**, 116-128.
76. M. Huš, D. Kopač and B. Likozar, *Journal of Catalysis*, 2020, **386**, 126-138.